ACS APPLIED NANO MATERIALS

www.acsanm.org

Article

Lithography-Free Ultrathin Lossless All-Dielectric Material with Magnetic Activity

Javier Alonso López Medina, Edwin Moncada Villa, Pedro Pizá, David Domínguez, Jorge Luis Vázquez Arce, Carlos Arturo Parra Vargas, Indry Milena Saavedra Gaona, Eval Baca Miranda, Osvaldo N. Oliveira, Jr, Mario H. Farías, Hugo Tiznado Vazquez,* and Jorge Ricardo Mejía-Salazar*

Cite This: ACS Appl. Nano Mater. 2025, 8, 4441−4452

Read Online

ACCESS | Metrics & More | Article Recommendations | Supporting Information

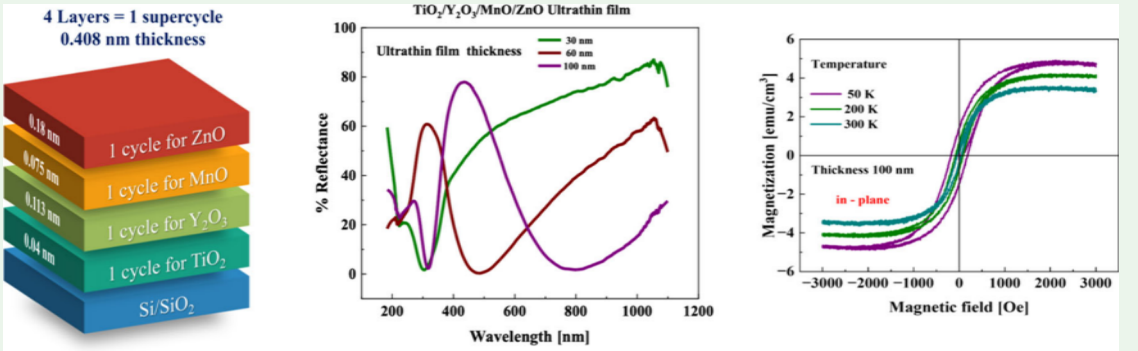

ABSTRACT: We report the fabrication of an ultrathin, lossless, all-dielectric ferromagnetic film via the sequential deposition of TiO_2/Y_2O_3/MnO/ZnO (TYMZO) monolayers on silicon (100) substrates by using atomic layer deposition (ALD). The TYMZO films, with controlled thicknesses of 30, 60, and 100 nm, exhibit tunable optical and structural properties. Their composition and structural integrity were confirmed using spectroscopic ellipsometry, UV−vis spectrophotometry, X-ray photoelectron spectroscopy (XPS), and transmission electron microscopy (TEM). The extinction coefficient of TYMZO approached zero across the optical spectrum, attributed to the lossless optical properties of its constituent materials. Cross-sectional TEM analysis revealed amorphous phases in films deposited at a substrate temperature of 250 °C, with a well-defined film−substrate interface. The amorphous nature of the TYMZO film, coupled with atomic migration of Ti and Mn, facilitated the formation of ZnO, TiO, and Y_2O_3 clusters as well as the potential formation of Mn-ZnO and Ti-ZnO compounds, which are known for their anisotropic magnetic properties. Magnetic measurements confirmed anisotropic ferromagnetic behavior, likely resulting from Mn-ZnO and Ti-ZnO clusters with nonparallel easy axes. The TYMZO films on silicon exhibited exceptional absorption efficiency across a tunable range of wavelengths. This enhanced absorption is attributed to the localization of optical fields within the lossless TYMZO layer due to Fabry−Perot resonances, which are subsequently absorbed by the lossy silicon substrate. These findings demonstrate the potential of TYMZO films for advanced photonic and magnetic applications, combining lossless optical properties with tunable ferromagnetic behavior.

KEYWORDS: *High-efficient absorber, Ultrathin film, Dielectric materials, Optical properties, Atomic layer deposition, amorphous phases, anisotropic ferromagnetic*

1. INTRODUCTION

Magnetophotonics and magnetoplasmonics[1,2] have been explored in such applications as in biosensing,[3−5] information storage/processing,[6] telecommunications,[7] and filtering.[8] One special difficulty for these applications is related to large optical losses due to Joule heating in the metals normally employed in the nanostructures. Attempts to overcome this drawback include the use of transparent conductive oxide nanocrystals[9] and metamaterials,[10−13] but the losses—though lower than in metallic ferromagnetic materials—remain relatively high in these dielectric garnet-based ferromagnetic materials.[14] Also, garnet-based dielectric materials tend to be bulky with high roughness and require complex and expensive techniques to be incorporated into chips through CMOS (complementary metal-oxide semiconductor) technology, thus hindering device miniaturization.[15] This is, in part, due to the mismatch of lattice parameters.

Received: November 19, 2024
Revised: February 12, 2025
Accepted: February 12, 2025
Published: February 22, 2025

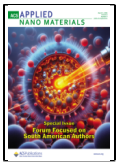

Efforts to integrate ferromagnetic semiconductors into CMOS technology have also explored diluted magnetic semiconductors (DMS), i.e., transition-metal (TM)-doped semiconducting oxides, such as In_2O_3 and ZnO,[16−20] which have shown promise for room-temperature spintronic applications.[21] However, these approaches face considerable challenges. For instance, increasing the TM doping concentration often results in higher conductivity,[19] which leads to increased losses. Additionally, producing cobalt-doped, ultrathin two-dimensional van der Waals ZnO films involves complex processes, such as dispersion in aqueous solutions, drying, and annealing.[22] Studies show that the physical properties of these materials are highly sensitive to annealing temperatures,[23] which can compromise reproducibility and stability. Consequently, the search for dielectric materials with inherent ferromagnetic properties and minimal losses remains an open research challenge.

In this work, we developed a new lossless all-dielectric optical material comprising atomically thin monolayers of TiO_2, Y_2O_3, MnO, and ZnO, referred to as TYMZO. Each of these dielectric materials has been recognized for their low toxicity, high stability, cost-effectiveness, optical and electrical properties, and seamless integration with CMOS technology.[24−26] The samples were fabricated using the atomic layer deposition (ALD) technique, with layers of each material deposited sequentially. Samples with nominal thicknesses of 30, 60, and 100 nm were produced. The fabricated TYMZO film demonstrated ferromagnetic properties comparable to those achieved through more complex recent methods.[22] However, a key advantage of our approach is its near-zero loss performance. Additionally, considering the magneto-optical Kerr effect (MOKE) measurements reported in ref 22, we anticipate that our idea could enable higher MOKE amplitudes due to the absence of losses—a goal pursued by many research groups in recent years. All samples exhibited high-refractive-index characteristics, leading to Fabry−Perot-like resonances (thoroughly discussed in the Supporting Information) that confine the optical field within the film. The latter is interesting since ultrathin optical absorbers are essential for compact optoelectronic and photonic devices, utilized in light harvesting,[27,28] photodetection,[29,30] modulation,[31] sensing,[32] and thermal light sources.[33] Several strategies have been applied to fabricate ultrathin, highly absorbing structures,[34−37] but they normally employ expensive techniques such as electron-beam (*e*-beam) lithography and focused ion beam (FIB) milling, limiting their adoption, particularly when nanostructures with complex geometries are required.[38,39] Two-dimensional materials like graphene and transition metal dichalcogenides (e.g., WS_2) are promising to overcome such limitations, owing to their small thickness and absorbing properties.[40,41] However, their application has been hampered by the difficulty in tuning their operating frequency bands. An alternative to obtain tuning of the absorption band is to employ all-dielectric ultrathin films functioning as Fabry−Perot resonators with optical fields concentrated on the highly absorbing materials. This approach permits tuning the absorption band through precise engineering of the ultrathin film using cost-effective, lithography-free techniques.[42] Here, we exploit a similar mechanism by controlling the thickness of the TYMZO ultrathin film on an absorbing silicon substrate. This allows tuning of the spectral position of the reflectance dip. The optical absorption capabilities of the structures were validated through numerical simulations. Significantly, the TYMZO films produced here are not only compatible with CMOS technology but also represent a new route for manufacturing lossless magneto-optical materials.

2. EXPERIMENTAL SECTION

2.1. Ultrathin Film Fabrication. Ultrathin films were grown at 250 °C substrate temperature on Si(100) wafers using thermal ALD with a Beneq model TFS-200 ALD viscous-flow reactor. The precursors used to fabricate TYMZO structures were tetrakis-(dimethylamino)titanium(IV) (TDMAT) at 60 °C, tris-(methylcyclopentadienyl)yttrium ($(MeCp_3)_3Y$) at 140 °C, bis-(ethylcyclopentadienyl)manganese $[(C_2H_5)C_5H_4]_2Mn$ at 60 °C, and diethylzinc at room temperature; all precursors were purchased from Strem Chemicals. Deionized water served as a reactant agent, and ultrahigh purity (UHP) N_2 purified to $<10^{-6}$ ppm of O_2 was the carrier/purging gas. TiO_2, Y_2O_3, and MnO precursors in the hot source containers were gradually heated and stabilized to prevent condensation. Since ALD enables precise control over materials properties,[43] in our experimental setup we fabricated ultrathin film structures of 70, 134, and 232 supercycles with the four distinct materials. The average total thicknesses were 28.9 nm (nominally 30 nm), 55.0 nm (nominally 60 nm), and 94.6 nm (nominally 100 nm), as illustrated in Figure 1a,b. The ALD pulse sequence to fabricate the samples is given in Table 1, specifying the dose and purge times for the ALD cycle (precursor, purge, reactant agent, purge) in preparing an ultrathin film with Ti, Y, Mn, and Zn single oxides. According to their nominal thickness, samples are named TYMZO − 30 nm, TYMZO − 60 nm, and TYMZO − 100 nm.

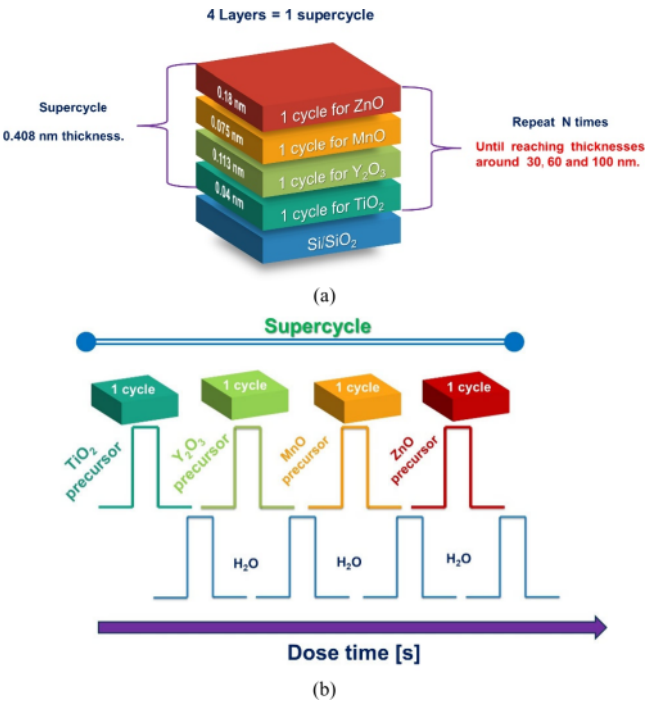

Figure 1. Schematic illustration of TYMZO samples produced by thermal ALD using a supercycle with four distinct materials, with total thicknesses of approximately 30, 60, and 100 nm. (b) ALD sequence scheme to produce thin films from TiO_2, Y_2O_3, MnO, and ZnO organometallic precursor.

2.2. Ultrathin Film Characterization. The TYMZO ALD films were characterized using spectroscopic ellipsometry (SE) with a spectroscopic ellipsometer (VASE) from Woollam Co, with which their thickness and optical properties were determined. SE measurements were conducted across a spectral range of 240−1000 nm at four incidence angles: 45°, 55°, 65°, and 75°. UV−vis spectra of the TYMZO films were recorded in reflectance mode at room

https://doi.org/10.1021/acsanm.4c06418
ACS Appl. Nano Mater. 2025, 8, 4441−4452

Table 1. Pulse Precursor Sequences Used in ALD to Obtain Monolayers

Precursor	Dose [ms]	Purge [s]	Layer	*GPC [Å/c]	Nominal layer thickness [nm]
TDMAT	75	1	TiO_2	0.40	0.04
H_2O	100	2			
$(MeCp_3)_3Y$	1	2	Y_2O_3	1.13	0.113
H_2O	100	3			
$[(C_2H_5)C_5H_4]_2Mn$	250	2	MnO	0.75	0.075
H_2O	150	3			
DEZ	50	1	ZnO	1.80	0.18
H_2O	100	1			
			Total Thickness for 1 layer		0.408 nm

*GPC: Grown per cycle

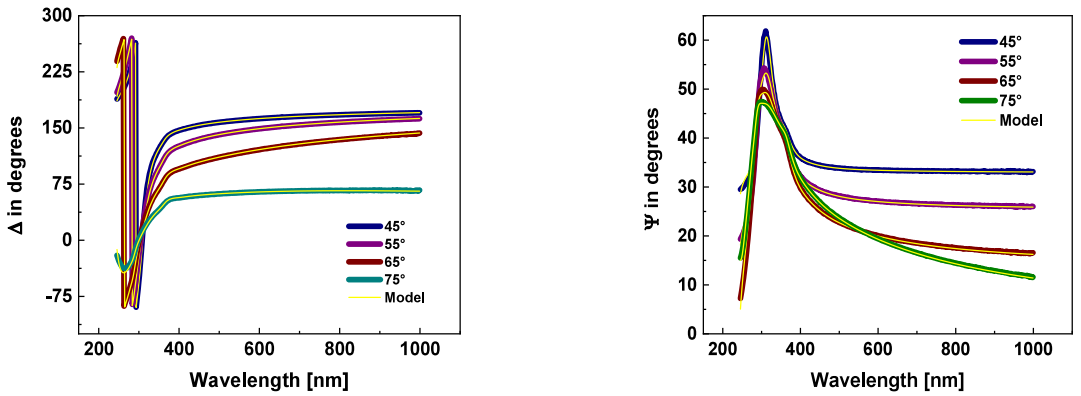

(a) (b)

Figure 2. Spectroscopic ellipsometry (VASE) and model data for a 30 nm thick TYMZO ultrathin film. (a) Δ and (b) Ψ ellipsometry angles obtained from EMA layer model.

temperature using an R/T AvaSpec-2048 Fiber Optic Spectrometer, equipped with both halogen and deuterium light sources, covering a scanning range from 200 to 1100 nm in the reflectance diffuse mode. X-ray photoelectron spectra (XPS) were taken with a SPECS GmbH custom-made system using a PHOIBOS 150 WAL hemispherical analyzer and a μ-FOCUS 500 X-ray source. All data was acquired using monochromated Al Kα X-rays (1486.6 eV, 110 W), a pass energy of 20 eV, and high-intensity lens mode. The diameter of the area analyzed was 0.88 mm. The vacuum chamber had a pressure below 2×10^{-9} mTorr. Charge referencing was done against adventitious carbon by setting the C 1s peak maximum at 284.8 eV. Spectra are presented with intensity in counts-per-second (CPS). The magnetic moment of all samples was measured as a function of the external magnetic field by using a Quantum Design vibrating sample magnetometer (VSM). Magnetization loops were recorded over a temperature range from 50 to 390 K, with an applied field ranging from −30 to 30 kOe. Film morphology was studied by scanning transmission electron microscopy (STEM) using a Hitachi HT 7700 microscope equipped with an EDS detector for elemental analysis. To observe the sample in the STEM mode, it was necessary to thin the ultrathin film through a sample preparation process in a JEM-9320FIB focused ion beam system (FIB) with a liquid gallium ion source. Before FIB preparation, the sample was coated with Au and carbon layers to avoid damage during the process. Also, STEM micrographs in the cross-sectional mode were used to validate the total ultrathin film thickness.

3. RESULTS AND DISCUSSION

3.1. Optical Studies. The ability to produce controlled ultrathin film using ALD was demonstrated with TYMZO ultrathin film of different thicknesses, which were determined using spectroscopic ellipsometry (SE). The total thickness and the $n(\lambda)$ and $k(\lambda)$ values corresponding to the optical parameters[43−45] were determined using a theoretical dispersion model that fits the SE results. Each TYMZO film was taken as a monolithic block made with one cycle of single oxide monolayers (TiO_2, Y_2O_3, MnO, and ZnO) in repeated sequence until a total thickness of around 30, 60, and 100 nm was reached (as nominal thickness). The single oxides were placed over a native SiO_2 layer that was 1.83 nm thick on a thicker Si(100) substrate; this native oxide growth is due to the exposure of the silicon wafer substrate to the ambient atmosphere. We used the effective medium approximation (EMA) model to calculate the optical constants for a mixed material, with the optical constants of two or more constituent materials being mixed. This model is useful for modeling surface and interfacial roughness, in addition to representing polycrystalline materials where optical constants of amorphous and crystalline materials are mixed. In our case, the optical model fits the experimental data with a small mean square error (MSE) for all samples. Thus, the total film thickness and the calculated optical constants are considered reliable. MSE was used to quantify the difference between experimental and theoretical data obtained with modeling ellipsometry results. The fitting model returns an MSE < 6. Figure 2a,b shows the measured and EMA model data to obtain the ellipsometry angles Ψ and Δ for the 30 nm thick sample (TYMZO − 30 nm). A similar behavior was observed for 60 and 100 nm samples as shown in Figure S1. In addition, the ultrathin film thicknesses obtained via spectroscopic ellipsometry measurements from the EMA optical model were 30, 55, and 95 nm, which are given in Table 2. These values demonstrate precise control over the layer growth, which is a characteristic feature of highly controlled deposition techniques such as ALD.

The optical parameters, specifically the refractive index $n(\lambda)$ and the extinction coefficient $k(\lambda)$, within the spectral range of 240−1100 nm, were determined using the effective medium approximation (EMA) model applied to spectroscopic

https://doi.org/10.1021/acsanm.4c06418
ACS Appl. Nano Mater. 2025, 8, 4441−4452

Table 2. Total Thickness of the TYMZO Ultrathin Film Evaluated by SE and TEM Measurements

Sample	Total Thickness		
	Nominal thickness [nm]	By SE [nm]	By TEM [nm]
TYMZO – 30 nm	30	30	32
TYMZO – 60 nm	60	55	58
TYMZO – 100 nm	100	95	92

ellipsometry data. Figure 3a,b shows the refractive index and extinction coefficient of TYMZO films deposited at 250 °C. The analysis of the ellipsometry data using the EMA model revealed a systematic decrease in the refractive index as the film thickness was reduced from 95 to 55 nm and further to 30 nm. Specifically, for the 30 nm thick film, the refractive index monotonically decreased from 2.40 to 1.75 over the 300−900 nm wavelength range. A similar trend was observed for the 55 nm (2.42 to 1.97) and 95 nm (2.40 to 2.00) thick films within the same spectral range. A comparable thickness-dependent behavior was observed in extinction coefficient $k(\lambda)$. For the 32 nm film, $k(\lambda)$ decreased from 0.18 to 0.003, while for the 58 and 92 nm films, it reduced from 0.17 to 0.007 and from 0.17 to 0.01, respectively. These findings indicate that both the refractive index and the extinction coefficient systematically decrease with decreasing film thickness, highlighting the significant influence of thickness on the optical properties of TYMZO thin films.

These results demonstrate that the optical properties of the ultrathin film can be tuned and tailored for specific applications. For example, the UV−vis spectra in Figure 4 show that it is possible to tune the reflection peaks by varying the ultrathin film thickness. Indeed, reflection peaks appear at 240, 300, and 410 nm for 30, 60, and 100 nm thick TYMZO films. The peak for the 30 nm ultrathin film is small, while the others are intense and broad. The reflection peak shifts toward shorter wavelengths as the total ultrathin film thickness decreases. The decrease in reflection as film thickness decreases from 100 to 30 nm may be explained by the electromagnetic field localization inside the ultrathin film due to multiple reflections at the top and bottom boundaries. This will be demonstrated numerically below using exact calculations with the scattering matrix method (SMM).[46] As the layer thickness varies, the phase of the optical fields changes, causing constructive or destructive interference between the internally reflected fields. This interference alters the wavelength at which reflectance peaks and dips occur, depending on the distance traversed by reflected light at the layer interfaces.

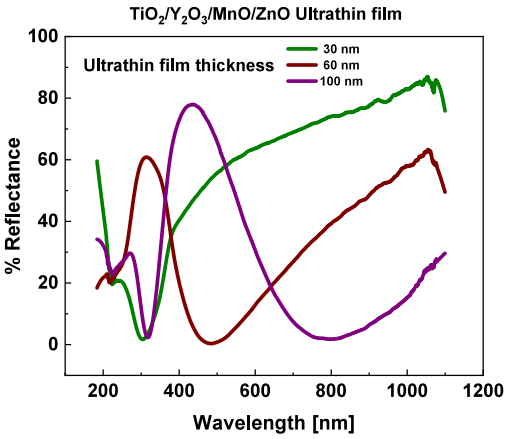

Figure 4. UV−Vis spectra for an ultrathin film with different thicknesses.

For a consistent explanation of the reflectance dips observed experimentally, we performed simulations using the SMM.[46] Numerical data of reflectance ($\boldsymbol{R}$), transmittance ($\boldsymbol{T}$), and absorbance ($\boldsymbol{A}$) were obtained for the ultrathin films in the wavelength range from 200 to 1000 nm, as shown in Figure 5a−c. Rather than using the experimental values for the fabricated films, these simulations utilize experimental refractive index data (as a function of the incident wavelength) for each individual film. We used the refractive indices of TiO_2, Y_2O_3, MnO, and ZnO to model the elementary unit cell of the ultrathin film. The thickness of the individual building layers, taken from Table 1, was used to construct a single cycle of each material. As represented in Figure 1, this elementary cell was repeated to achieve the total thicknesses of 100, 60, and 30 nm. Reflectance measurements were conducted under normal incidence, and calculations were performed for an incident angle $\theta = 0°$ for comparative purposes. The excellent qualitative agreement between experimental and numerical results for reflectance indicates that the minima in $\boldsymbol{R}$ is associated with high absorbance favored by Fabry−Perot resonance in the ultrathin film, as explained in the Supporting Information. Differences in the simulated and measured reflectance spectra can be explained by the lossy models for the TiO_2, Y_2O_3, MnO, and ZnO building materials in the

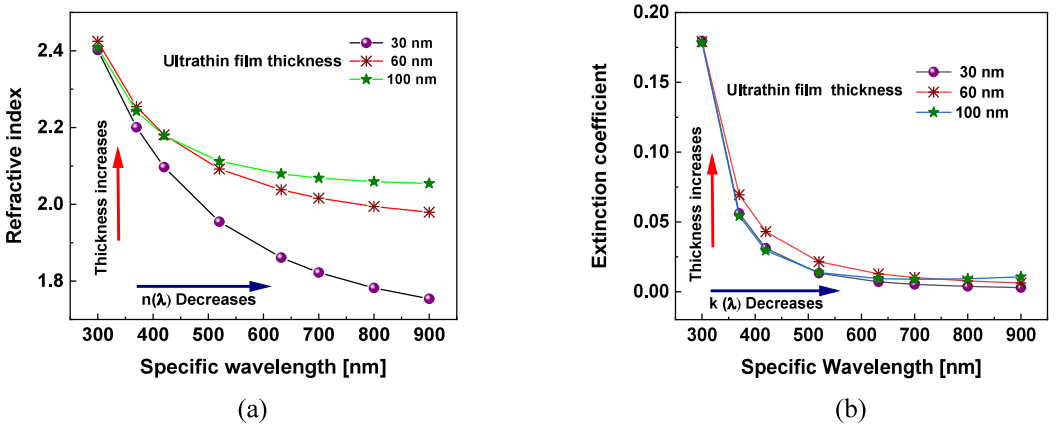

Figure 3. Optical parameters for TYMZO ultrathin film. (a) Refractive index profile $n(\lambda)$ and (b) extinction coefficient $k(\lambda)$ as functions of the incident wavelength for different thicknesses.

https://doi.org/10.1021/acsanm.4c06418
ACS Appl. Nano Mater. 2025, 8, 4441−4452

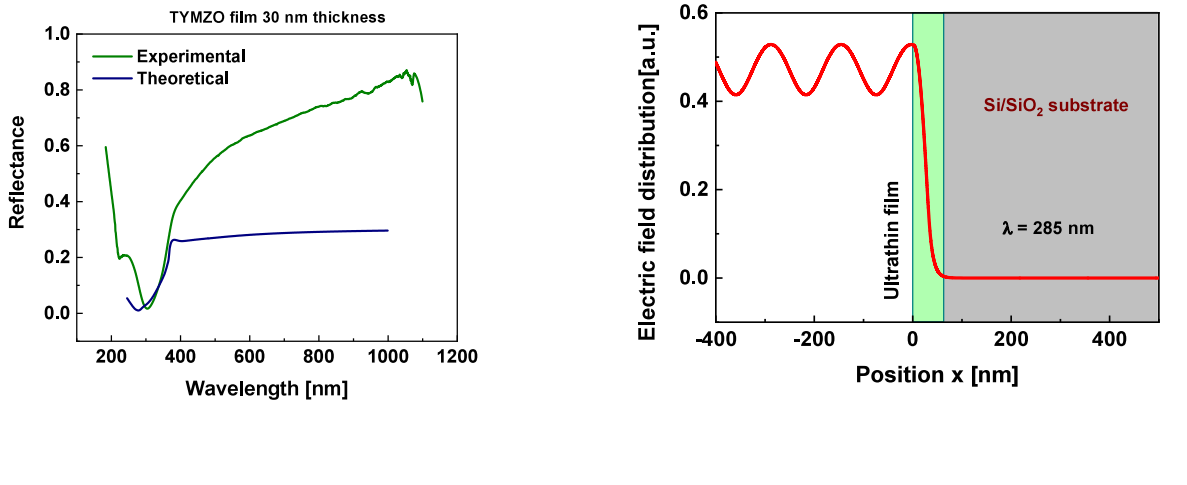

(a)

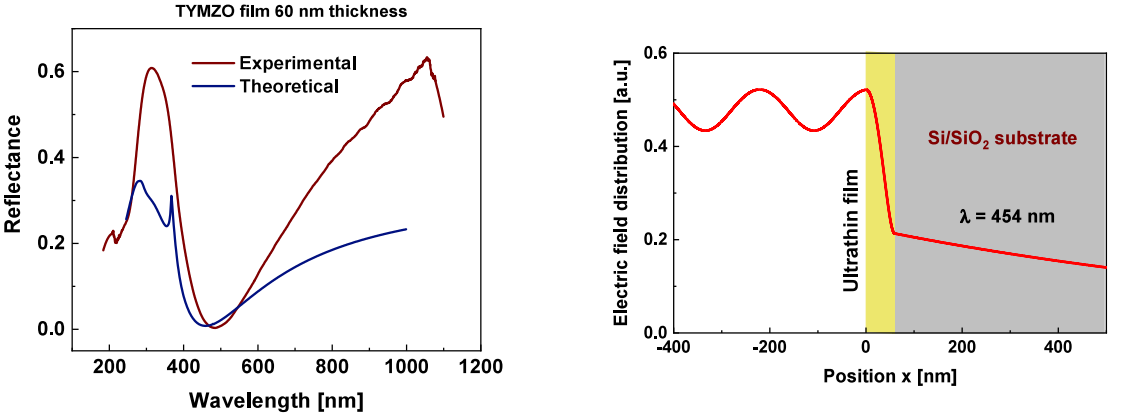

(b)

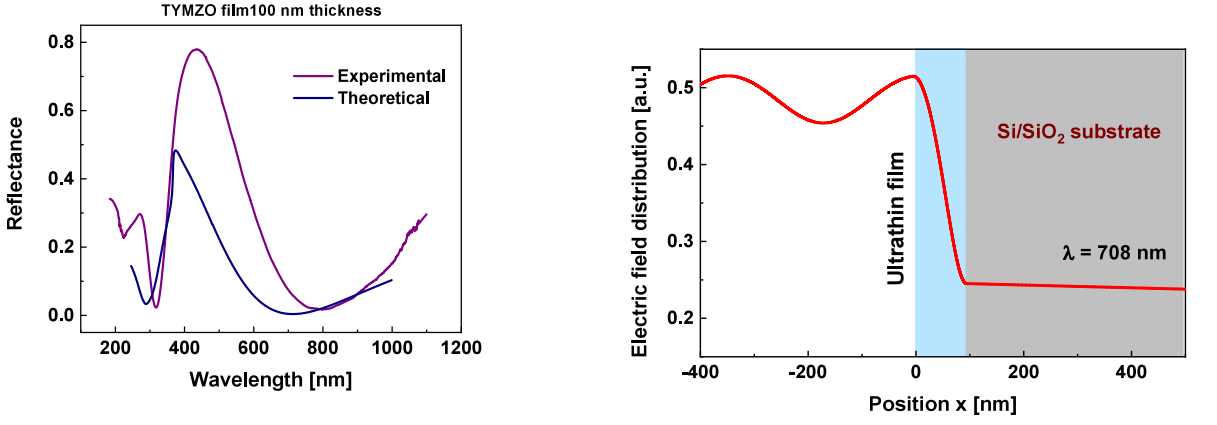

(c)

Figure 5. Optical response simulation and electrical field distribution for TYMZO ultrathin film whose thickness is (a) 30 nm, (b) 60 nm, and (c) 100 nm.

simulations, while ellipsometry results indicate a lossless behavior for the fabricated sample (corroborated by higher reflectance amplitudes far from the Fabry−Perot resonances). The absorption of electromagnetic energy is further supported by the electric field profiles shown on the right-hand side panel in Figure 5a−c. The evanescent behavior indicates that the

https://doi.org/10.1021/acsanm.4c06418
ACS Appl. Nano Mater. 2025, 8, 4441−4452

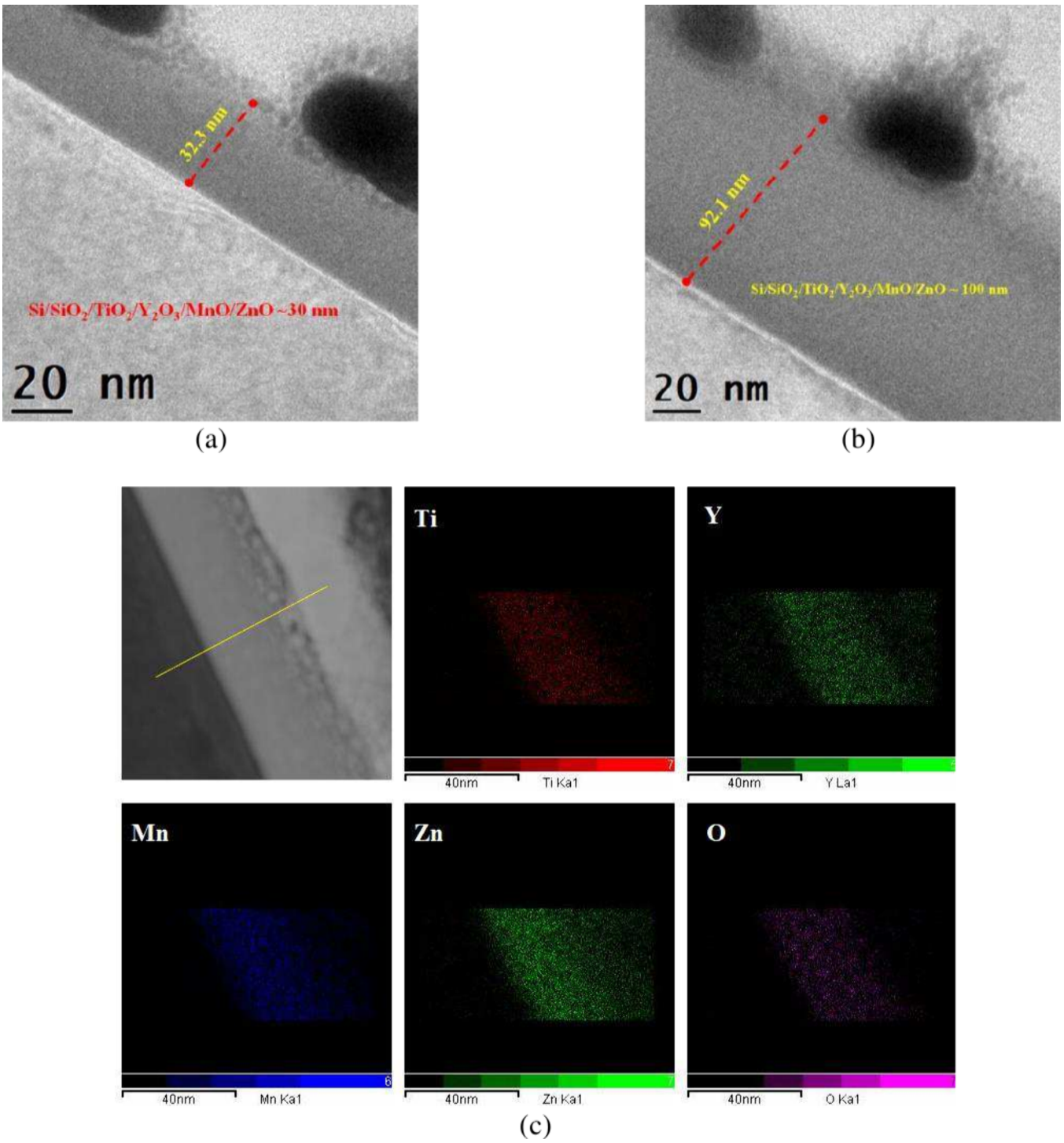

Figure 6. Cross-sectional measurements. TEM images for (a) 30 and (b) 100 nm nominal thickness for TYMZO ultrathin film. (c) Chem-map from STEM with energy dispersive X-ray spectroscopy (EDX) for TYMZO to visualize each element distribution in the film (Ti in red color, Y in green, Mn in blue, Zn in green, and O in violet).

physical principle behind the absorbing features of TYMZO lies in the light confinement within the high-refractive-index film, which is subsequently absorbed by the Si substrate. Although analogous approaches can be found in the literature, the extraordinary feature of our concept lies in the ferromagnetic behavior of the fabricated ultrathin film, as demonstrated in the next section.

3.2. Morphological Studies. The precision of ALD in producing films with controlled thickness at the nanoscale was confirmed with TEM images, which also proves the ultrathin film uniformity. Figure 6a,b shows a TEM image for ∼30 and ∼100 nm TYMZO ultrathin films. The TEM transversal section allows for distinguishing the interface between the substrate and deposited layers. The cross-sectional structure for both samples deposited at a 250 °C substrate temperature shows amorphous phases. Since the temperature in the ALD reactor was relatively low, there is no crystallization in TiO_2, Y_2O_3, MnO, and ZnO[47] under these conditions (pressure,

https://doi.org/10.1021/acsanm.4c06418
ACS Appl. Nano Mater. 2025, 8, 4441−4452

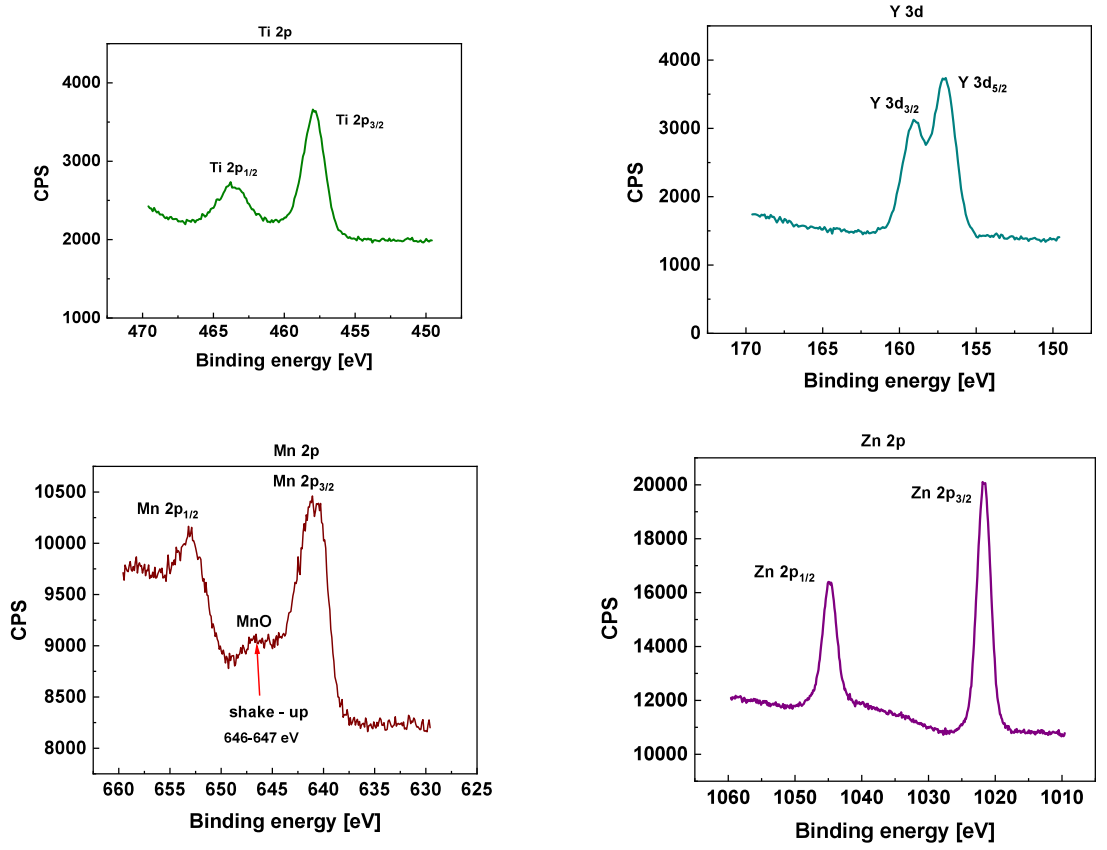

Figure 7. XPS high-resolution spectra of Ti 2p. Y 3d, Mn 2p, and Zn 2p for TYMZO ultrathin film with 100 nm total thickness.

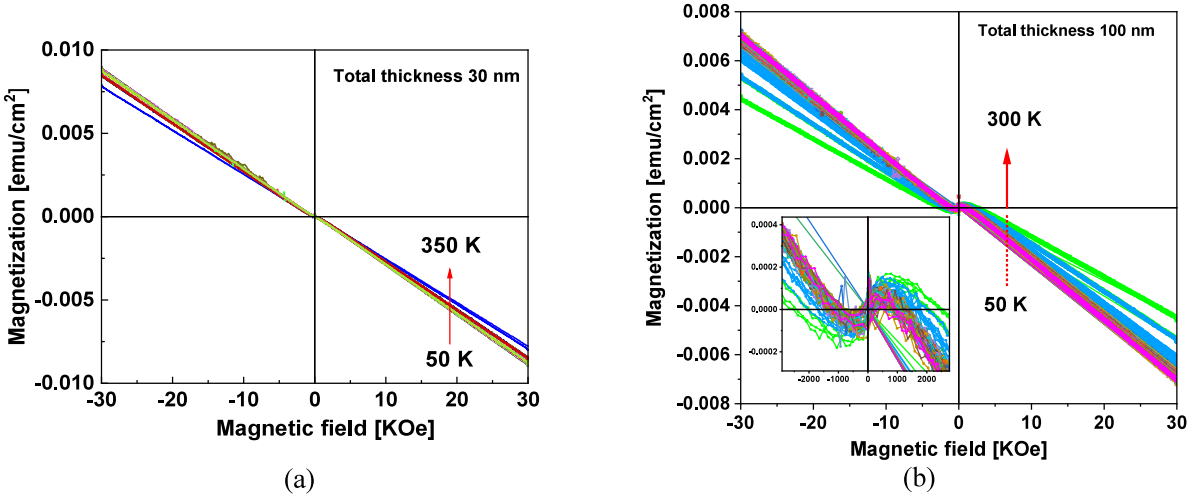

Figure 8. Magnetic response measured for TYMZO films deposited on Si(100) substrates, at temperatures ranging from 50 to 350 K for the 30 nm film (a) and from 50 to 300 K for the 100 nm film (b).

deposition temperature, precursor temperature, and inert gas flux). In addition, a well-defined interface is seen in the TEM images between the layers and the boundary with the silicon substrate. The thicknesses estimated from TEM images are consistent with expected values from SE measurements, ∼ 32, 58, and 92 nm. Figure 6c shows a chemmap from STEM measurements with energy dispersive X-ray spectroscopy (EDX) for a TYMZO film prepared at 250 °C by ALD for studying the possible segregation of different elements. The presence and distribution of chemical elements are shown in false-color X-ray emission associated with Ti (in red), Y (in green), Mn (in blue), Zn (in green), and O (in violet). A larger amount of Zn is observed because the deposition rate for the zinc precursor (DEZ) in a single ALD cycle (Table 1) is much higher than for the chemical precursors for Ti, Mn, and Y oxides.

3.3. Physicochemical Studies. The high-resolution spectra of the five constituent elements, *viz.* Ti 2p, Y 3d, Mn 2p, and Zn 2p of the 100 nm TYMZO film shown in Figure 7 indicate the presence of the four metals in the film. Similar intensities and peak shapes were observed in all three samples (30, 60, and 100 nm). This is because the XPS signal originates

https://doi.org/10.1021/acsanm.4c06418
ACS Appl. Nano Mater. 2025, 8, 4441−4452

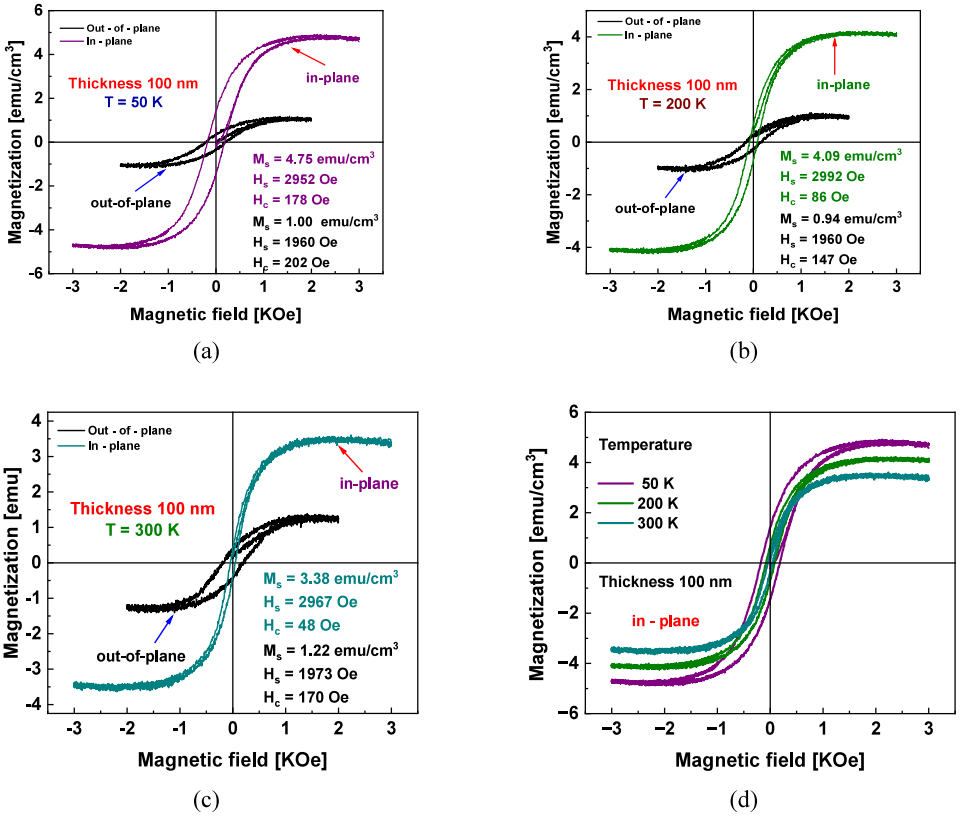

Figure 9. Magnetic behavior for the 100 nm thick $TiO_2/Y_2O_3/MnO/ZnO$ film, in-plane and out-of-plane, for different temperatures: (a) 50 K, (b) 200 K, (c) 300 K; (d) comparison of the magnetic behavior at different temperatures for in-plane configuration.

from the surface and is approximately 2 nm deep. Since each single layer in a supercycle of the four oxides is about 0.408 nm thick, XPS provides information from multiple layers, similarly across all samples. A broad signal within the binding energy region between 644 and 648 eV of Mn 2p indicates the characteristic satellite peak associated with Mn^{2+}. Although manganese can exist in up to six stable oxidation states, only Mn^{2+} is accompanied by a satellite signal in this energy range. Therefore, in all three TYMZO samples, manganese predominantly exists in the Mn^{2+} oxidation state. For Zn 2p, the energy difference between $2p_{1/2}$ and $2p_{3/2}$ is 23.11 eV, indicative of the Zn^{2+} oxidation state. The spectral shapes for Y 3d and Ti 2p are closely associated with their most stable oxidation states, Y^{3+} and Ti^{4+}. The energy difference between Y $3d_{3/2}$ − Y $3d_{5/2}$ and Ti $2p_{1/2}$ − Ti $2p_{3/2}$ were determined to be 2.05 and 4.72 eV, respectively.[48−56]

3.4. Magnetic Properties of TYMZO Ultrathin Film.

The magnetic response between ±30 kOe for 30 and 100 nm TYMZO films deposited on Si(100) substrates exhibits a distinct ferromagnetic component at low magnetic fields. However, at higher fields, this behavior is dominated by the diamagnetic nature of the Si substrate, as illustrated in Figure 8a,b. The ultrathin films display a notable anisotropic magnetic response, characterized by a preferential in-plane magnetization direction. The amorphous phases of these TYMZO ultrathin films suggest the possible formation of nanoclusters composed of TiO_2, Y_2O_3, MnO, and ZnO oxides, which feature interacting surfaces and quasi-bidimensional structures.[57,58] These surfaces, associated with the dangling bonds of the amorphous matrix, may promote the migration of TM atoms, facilitating the formation of TM-doped oxides. Specifically, Mn-doped ZnO, Ti-doped ZnO, and TiO or TiO_2 DMSs exhibit semiconducting properties with remarkable anisotropic ferromagnetic features.[59−61] A fundamental characteristic of DMSs is the *sp*−*d* coupling between free carriers and the localized *d*-electrons of TM dopants, which underpins the magnetic behavior of these materials.[58,62] In this context, *p*−*d* coupling, determined by *p*−*d* hybridization, varies with the TM *d*-electrons, while *s*−*d* coupling remains constant. The *d*-orbital of a substitutional TM ion in a zinc blende crystal structure splits into an e_2 doublet and a t_2 triplet, with both energy states possibly residing within the oxide bandgap. Contrary to conventional ferromagnets, the magnetization anisotropy in diluted magnetic oxides, both doped and undoped, remains only partially understood.[59,62−64]

The magnetic hysteresis loops reported in this study reveal possible magnetization contributions from TiO, TiO_2, Mn-doped ZnO, and Ti-doped ZnO films. Literature sources corroborate the in-plane and out-of-plane magnetization for TiO[60] and the in-plane magnetization for Mn-doped ZnO[65,66] and Ti-doped ZnO[61] materials. In our experiments, hysteresis loops were measured in both in-plane and out-of-plane geometries at 50, 200, and 300 K. After subtracting the diamagnetic contribution of the substrate, ferromagnetic M(H) loops were observed. Figure 9a−d displays the ferromagnetic loops of the ∼92 nm (100 nm nominal thickness) thick film in the range from −2000 to +2000 Oe. The in-plane hysteresis loops were significantly larger than the out-of-plane loops across the 50−300 K temperature range, confirming the pronounced anisotropic behavior and preferential in-plane magnetization. Key parameters of the in-plane measurements, such as the squareness ratio (M_r/M_s),

https://doi.org/10.1021/acsanm.4c06418
ACS Appl. Nano Mater. 2025, 8, 4441−4452

saturation magnetization (M_s), and coercive field (H_c), show a strong temperature dependence, decreasing sharply with increasing temperature. This trend suggests a superparamagnetic behavior. Conversely, the out-of-plane parameters remained nearly constant with the temperature. The XPS high-resolution spectra of Ti 2p. Y 3d, Mn 2p, and Zn 2p values for the 100 nm TYMZO film can be proof of the formation of some Mn-doped ZnO clusters into the film. However, other experiments, such as spin paramagnetic resonance (SPR), are necessary to substantiate these assertions.

4. CONCLUSIONS

Using the lithography-free ALD technique, we demonstrated a new approach to fabricating ultrathin lossless dielectric ferromagnetic films. Our approach consists of using atomically thin transparent semiconductor-oxide layers of CMOS-compatible materials. We also show that varying the film thickness allows one to tune the optical properties. By depositing the ultrathin film on a lossy silicon substrate, we observed an exceptional absorption of light. The wavelength associated with the maximum absorption peak can be tuned by changing the layer thickness, as proven both experimentally and theoretically. This mechanism was attributed to Fabry–Perot-like resonances in the high-refractive-index dielectric layers. From the optical response of the ultrathin film, we noticed that the refractive index decreased from 2.40 to 1.75 between 300 and 900 nm for the 30 nm thick sample. A similar behavior was observed for the 60 nm (from 2.42 to 1.97) and 100 nm thick (from 2.4 to 2.0) samples. With the possible control of ultrathin film optical properties, tailored applications can now be sought in various domains, such as sensing and magnetometry. An anisotropic ferromagnetic behavior was observed for the TYMZO films, probably caused by Mn-ZnO and Ti-ZnO clusters with nonparallel easy axes.

■ ASSOCIATED CONTENT

Data Availability Statement

The data that support the findings of this study are available from the corresponding author upon reasonable request.

Supporting Information

The Supporting Information is available free of charge at https://pubs.acs.org/doi/10.1021/acsanm.4c06418.

A comprehensive analytical and numerical study confirming that the resonances observed in the developed ultrathin film are Fabry–Perot resonances; to provide a deeper understanding of the resonant behavior, these analyses examine both the lossy and ideal lossless cases (PDF)

■ AUTHOR INFORMATION

Corresponding Authors

Hugo Tiznado Vazquez − *Centro de Nanociencias y Nanotecnología, Universidad Nacional Autónoma de México, Ensenada, B.C. 22800, México*; Email: tiznado@ens.cnyn.unam.mx

Jorge Ricardo Mejía-Salazar − *Instituto Nacional de Telecomunicações (Inatel), Santa Rita do Sapucaí, MG 37540-000, Brasil*; orcid.org/0000-0003-1742-9957; Email: jrmejia@inatel.br

Authors

Javier Alonso López Medina − *CONAHCYT − IxM - Centro de Nanociencias y Nanotecnología, Universidad Nacional Autónoma de México, Ensenada, B.C. 22800, México*; orcid.org/0009-0006-2146-5511

Edwin Moncada Villa − *Escuela de Física, Universidad Pedagógica y Tecnológica de Colombia, Tunja 150001, Colombia*

Pedro Pizá − *Centro de Investigación en Materiales Avanzados S. C, Chihuahua, CHIH 31136, México*

David Domínguez − *Centro de Nanociencias y Nanotecnología, Universidad Nacional Autónoma de México, Ensenada, B.C. 22800, México*

Jorge Luis Vázquez Arce − *Centro de Investigación Científica y Educación Superior de Ensenada-CICESE, Ensenada, B.C. 22860, México*

Carlos Arturo Parra Vargas − *Escuela de Física, Universidad Pedagógica y Tecnológica de Colombia, Tunja 150001, Colombia*

Indry Milena Saavedra Gaona − *Escuela de Física, Universidad Pedagógica y Tecnológica de Colombia, Tunja 150001, Colombia*

Eval Baca Miranda − *Grupo Ingeniería de Nuevos Materiales, Universidad del Valle, Cali 760042, Colombia*

Osvaldo N. Oliveira, Jr − *Instituto de Física de Sao Carlos, Universidade de Sao Paulo, Sao Carlos, SP 13560-970, Brasil*; orcid.org/0000-0002-5399-5860

Mario H. Farías − *Centro de Nanociencias y Nanotecnología, Universidad Nacional Autónoma de México, Ensenada, B.C. 22800, México*

Complete contact information is available at: https://pubs.acs.org/10.1021/acsanm.4c06418

Author Contributions

The contribution made in the manuscript by each author are presented below: **Javier Alonso López Medina:** Investigation, Writing - original draft, Visualization, Funding acquisition, Project administration. **Edwin Moncada Villa:** Investigation, Writing - original draft, Visualization. **Pedro Pizá Ruiz:** Investigation, Methodology, Visualization, Writing - original draft. **David Alejandro Domínguez Vargas:** Methodology, Visualization, Writing - review and editing. **Jorge Luis Vázquez Arce:** Investigation, Writing - original draft. **Carlos Arturo Parra Vargas:** Investigation, Methodology, Visualization. **Indry Milena Saavedra Gaona:** Methodology, Investigation, Writing - original draft. **Eval Baca Miranda:** Methodology, Investigation Writing - original draft. **Osvaldo N. Oliveira Jr.:** Methodology, Investigation, Writing - original draft, Funding acquisition, Project administration. **Mario H. Farias**: Methodology, Investigation, Visualization Writing - original draft, Funding acquisition, Project administration. **Hugo Tiznado**: Visualization, Writing - review and editing. **Jorge Ricardo Mejía Salazar**: Investigation, Writing - original draft, Writing - review and editing, Funding acquisition, Project administration.

Funding

The National Autonomous University of Mexico (UNAM) will cover the open-access publication fee for this article through an existing agreement with the journal. This agreement provides funding for the article processing charge (APC) for authors with UNAM affiliation, when the corresponding author uses an email address ending in @···unam.mx. This work was partially

supported by CONAHCYT Basic Science projects 2017−2018 A1-S-21323, A1-S-21084 and DGAPA-UNAM research projects: PAPIIT IN119023, IG100925, IN110424, and IG101124. Partial financial support was also received from RNP, with resources from MCTIC, under Grant 01250.075413/2018-04 and Grant 01245.010604/2020-14, under the 6G Mobile Communications Systems of the Radiocommunication Reference Center (Centro de Referência em Radiocomunicações-CRR) project of the National Institute of Telecommunications (INATEL), Brazil. Authors also acknowledge the financial support from the Brazilian agencies National Council for Scientific and Technological Development-CNPq, FAPEMIG (APQ-05305−23), and FAPESP (2018/22214-6).

Notes

The authors declare no competing financial interest.

■ ACKNOWLEDGMENTS

The authors express their sincere gratitude to Dr. Nicola Nedev for his invaluable assistance with ellipsometry measurements and to Francisco Ruíz for providing the TEM results.

■ REFERENCES

(1) Rizal, C.; Shimizu, H.; Mejía-Salazar, J. R. Magneto-Optics Effects: New Trends and Future Prospects for Technological Developments. *Magnetochemistry 2022, Vol. 8, Page 94* **2022**, *8* (9), 94.

(2) Rizal, C.; Manera, M. G.; Ignatyeva, D. O.; Mejía-Salazar, J. R.; Rella, R.; Belotelov, V. I.; Pineider, F.; MacCaferri, N. Magneto-photonics for Sensing and Magnetometry toward Industrial Applications. *J. Appl. Phys.* **2021**, *130* (23), 230901.

(3) Sarmiento, S. A.; Moncada-Villa, E.; Mejia-Salazar, J. R. Magnetically Tunable Brewster Angle in Uniaxial Magneto-Optical Metamaterials for Advanced Integration of High-Resolution Sensing Devices. *Optics Letters* **2024**, *49* (8), 1973−1976.

(4) Carvalho, W. O. F.; Oliveira, O. N.; Mejía-Salazar, J. R. Magnetochiroptical Nanocavities in Hyperbolic Metamaterials Enable Sensing down to the Few-Molecule Level. *J. Chem. Phys.* **2024**, *160* (7), 71104.

(5) Makarova, A. V.; Nerovnaya, A. A.; Gulkin, D. N.; Popov, V. V.; Frolov, A. Y.; Fedyanin, A. A. Goos-Hänchen Shift Spatially Resolves Magneto-Optical Kerr Effect Enhancement in Magnetoplasmonic Crystals. *ACS Photonics* **2024**, *11*, 1619.

(6) Ehrler, J.; He, M.; Shugaev, M. V.; Polushkin, N. I.; Wintz, S.; Liersch, V.; Cornelius, S.; Hübner, R.; Potzger, K.; Lindner, J.; Fassbender, J.; Ünal, A. A.; Valencia, S.; Kronast, F.; Zhigilei, L. V.; Bali, R. Laser-Rewriteable Ferromagnetism at Thin-Film Surfaces. *ACS Appl. Mater. Interfaces* **2018**, *10* (17), 15232−15239.

(7) Ho, K. S.; Im, S. J.; Pae, J. S.; Ri, C. S.; Han, Y. H.; Herrmann, J. Switchable Plasmonic Routers Controlled by External Magnetic Fields by Using Magneto-Plasmonic Waveguides. *Scientific Reports 2018 8:1* **2018**, *8* (1), 1−8.

(8) Morton, P.; Shoji, Y.; Bowers, J. E.; Zhang, C.; Pintus, P.; Mizumoto, T.; Huang, D. Dynamically Reconfigurable Integrated Optical Circulators. *Optica* **2017**, *4* (1), 23−30.

(9) Gabbani, A.; Sangregorio, C.; Tandon, B.; Nag, A.; Gurioli, M.; Pineider, F. Magnetoplasmonics beyond Metals: Ultrahigh Sensing Performance in Transparent Conductive Oxide Nanocrystals. *Nano Lett.* **2022**, *22* (22), 9036−9044.

(10) Ignatyeva, D. O.; Karki, D.; Voronov, A. A.; Kozhaev, M. A.; Krichevsky, D. M.; Chernov, A. I.; Levy, M.; Belotelov, V. I. All-Dielectric Magnetic Metasurface for Advanced Light Control in Dual Polarizations Combined with High-Q Resonances. *Nature Communications 2020 11:1* **2020**, *11* (1), 1−8.

(11) Wang, X.; Wang, H.; Jian, J.; Rutherford, B. X.; Gao, X.; Xu, X.; Zhang, X.; Wang, H. Metal-Free Oxide-Nitride Heterostructure as a Tunable Hyperbolic Metamaterial Platform. *Nano Lett.* **2020**, *20* (9), 6614−6622.

(12) Wang, X.; Jian, J.; Wang, H.; Liu, J.; Pachaury, Y.; Lu, P.; Rutherford, B. X.; Gao, X.; Xu, X.; El-Azab, A.; Zhang, X.; Wang, H. Nitride-Oxide-Metal Heterostructure with Self-Assembled Core-Shell Nanopillar Arrays: Effect of Ordering on Magneto-Optical Properties. *Small* **2021**, *17* (5), 2007222.

(13) Fan, B.; Nasir, M. E.; Nicholls, L. H.; Zayats, A. V.; Podolskiy, V. A. Magneto-Optical Metamaterials: Nonreciprocal Transmission and Faraday Effect Enhancement. *Adv. Opt Mater.* **2019**, *7* (14), 1801420.

(14) Carvalho, W. O. F.; Moncada-Villa, E.; Oliveira, O. N.; Mejía-Salazar, J. R. Beyond Plasmonic Enhancement of the Transverse Magneto-Optical Kerr Effect with Low-Loss High-Refractive-Index Nanostructures. *Phys. Rev. B* **2021**, *103* (7), 075412.

(15) Murai, T.; Shoji, Y.; Shoji, Y.; Nishiyama, N.; Nishiyama, N.; Mizumoto, T. Nonvolatile Magneto-Optical Switches Integrated with a Magnet Stripe Array. *Optics Express* **2020**, *28* (21), 31675−31685.

(16) Ando, K.; Saito, H.; Jin, Z.; Fukumura, T.; Kawasaki, M.; Matsumoto, Y.; Koinuma, H. Large Magneto-Optical Effect in an Oxide Diluted Magnetic Semiconductor Zn1-xCoxO. *Appl. Phys. Lett.* **2001**, *78* (18), 2700−2702.

(17) Philip, J.; Punnoose, A.; Kim, B. I.; Reddy, K. M.; Layne, S.; Holmes, J. O.; Satpati, B.; Leclair, P. R.; Santos, T. S.; Moodera, J. S. Carrier-Controlled Ferromagnetism in Transparent Oxide Semiconductors. *Nature Materials 2006 5:4* **2006**, *5* (4), 298−304.

(18) Varvaro, G.; Di Trolio, A.; Polimeni, A.; Gabbani, A.; Pineider, F.; De Julián Fernández, C.; Barucca, G.; Mengucci, P.; Amore Bonapasta, A.; Testa, A. M. Giant Magneto-Optical Response in H+ Irradiated Zn1-xCoxO Thin Films. *J. Mater. Chem. C Mater.* **2019**, *7* (1), 78−85.

(19) Kayani, Z. N.; Nazli, H.; Kousar, S.; Riaz, S.; Naseem, S. Dip-Coated V Doped ZnO Thin Films: Dielectric and Magnetic Properties. *Ceram. Int.* **2020**, *46* (10), 14605−14612.

(20) Awan, S. U.; Akhtar, M. T.; Hussain, D.; Shah, S. A.; Rizwan, S.; Rafique, M.; Samad, A.; Arshad, M. Defects Mediated Weak Ferromagnetism in Zn1-yCyO ($0.00 \leq y \leq 0.10$) Nanorods Semiconductors for Spintronics Applications. *Scientific Reports 2023 13:1* **2023**, *13* (1), 1−20.

(21) Weng, Z.; Huang, Z.; Lin, W. First-Principles Study of Ferromagnetism in Ti-Doped ZnO with Oxygen Vacancy. *Physica B Condens Matter* **2012**, *407* (4), 743−747.

(22) Chen, R.; Luo, F.; Liu, Y.; Song, Y.; Dong, Y.; Wu, S.; Cao, J.; Yang, F.; N'Diaye, A.; Shafer, P.; Liu, Y.; Lou, S.; Huang, J.; Chen, X.; Fang, Z.; Wang, Q.; Jin, D.; Cheng, R.; Yuan, H.; Birgeneau, R. J.; Yao, J. Tunable Room-Temperature Ferromagnetism in Co-Doped Two-Dimensional van Der Waals ZnO. *Nature Communications 2021 12:1* **2021**, *12* (1), 1−8.

(23) Abbady, G.; Afify, N.; Sedky, A.; Hamad, D. Effect of Annealing Temperature on Structural, Optical and Magnetic Properties of Cd1-XMnxZnO2 Nanocomposites: An Investigation for Ferromagnetic. *Ceram. Int.* **2023**, *49* (11), 18042−18054.

(24) Lee, J.; Seul, H.; Jeong, J. K. Solution-Processed Ternary Alloy Aluminum Yttrium Oxide Dielectric for High Performance Indium Zinc Oxide Thin-Film Transistors. *J. Alloys Compd.* **2018**, *741*, 1021−1029.

(25) Kaur, D.; Bharti, A.; Sharma, T.; Madhu, C. Dielectric Properties of ZnO-Based Nanocomposites and Their Potential Applications. *Int. J. Opt* **2021**, *2021* (1), 9950202.

(26) Xu, H.; Ding, X.; Qi, J.; Yang, X.; Zhang, J. A Study on Solution-Processed Y2O3 Films Modified by Atomic Layer Deposition Al2O3 as Dielectrics in ZnO Thin Film Transistor. *Coatings 2021, Vol. 11, Page 969* **2021**, *11* (8), 969.

(27) Çetinkaya, Ç.; Çokduygulular, E.; Kınacı, B.; Güzelçimen, F.; Özen, Y.; Sönmez, N. A.; Özçelik, S. Highly Improved Light Harvesting and Photovoltaic Performance in CdTe Solar Cell with Functional Designed 1D-Photonic Crystal via Light Management Engineering. *Scientific Reports 2022 12:1* **2022**, *12* (1), 1−12.

https://doi.org/10.1021/acsanm.4c06418
ACS Appl. Nano Mater. 2025, 8, 4441−4452

(28) Mattiotti, F.; Sarovar, M.; Giusteri, G. G.; Borgonovi, F.; Celardo, G. L. Efficient Light Harvesting and Photon Sensing via Engineered Cooperative Effects. *New J. Phys.* **2022**, *24* (1), 013027.
(29) Song, S.; Ma, X.; Pu, M.; Li, X.; Guo, Y.; Gao, P.; Luo, A. X. Tailoring Active Color Rendering and Multiband Photodetection in a Vanadium-Dioxide-Based Metamaterial Absorber. *Photonics Research* **2018**, *6* (6), 492−497.
(30) Kamal, S.; Bennett-Jackson, A.; Srivastava, R.; Bruce, R. C.; Ozaktas, E. G.; Khoury, C.; Budhani, R.; Shrekenhamer, D.; Thon, S. M. Plasmonically Enhancing 2D WSe2 Light Absorption for Photodetection. *MRS Adv.* **2024**, *9*, 628−633.
(31) Che, Y.; Wang, X.; Song, Q.; Zhu, Y.; Xiao, S. Tunable Optical Metasurfaces Enabled by Multiple Modulation Mechanisms. *Nanophotonics* **2020**, *9* (15), 4407−4431.
(32) Yu, Z.; Sun, X.; Feng, A. Ultranarrow-Band Metagrating Absorbers for Sensing and Modulation. *Optics Express* **2018**, *26* (22), 28197−28205.
(33) Kats, M. A.; Capasso, F. Optical Absorbers Based on Strong Interference in Ultra-Thin Films. *Laser Photon Rev.* **2016**, *10* (5), 735−749.
(34) Xu, R.; Fujikata, J.; Takahara, J.; Takahara, J. Graphene Perfect Absorber Based on Degenerate Critical Coupling of Toroidal Mode. *Optics Letters* **2023**, *48* (6), 1490−1493.
(35) Xu, R.; Takahara, J.; Takahara, J. All-Dielectric Perfect Absorber Based on Quadrupole Modes. *Optics Letters* **2021**, *46* (15), 3596−3599.
(36) Yu, P.; Besteiro, L. V.; Huang, Y.; Wu, J.; Fu, L.; Tan, H. H.; Jagadish, C.; Wiederrecht, G. P.; Govorov, A. O.; Wang, Z. Broadband Metamaterial Absorbers. *Adv. Opt Mater.* **2019**, *7* (3), 1800995.
(37) Hajian, H.; Ghobadi, A.; Serebryannikov, A. E.; Butun, B.; Vandenbosch, G. A. E.; Ozbay, E. Tunable Infrared Asymmetric Light Transmission and Absorption via Graphene-HBN Metamaterials. *J. Appl. Phys.* **2019**, *126* (19), 193102 DOI: 10.1063/1.5118887.
(38) Yuan, W.; Yu, Y.; Yu, X.; Tee, C. A. T.; Zhao, J.; Yang, X. Polarization-Independent and High-Efficiency Broadband Optical Absorber in Visible Light Based on Nanostructured Germanium Arrays. *Optics Letters* **2019**, *44* (4), 963−966.
(39) Li, Y.; Liu, Z.; Zhang, H.; Tang, P.; Wu, B.; Liu, A. G. Ultra-Broadband Perfect Absorber Utilizing Refractory Materials in Metal-Insulator Composite Multilayer Stacks. *Optics Express* **2019**, *27* (8), 11809−11818.
(40) Sreekanth, K. V.; Elkabbash, M.; Medwal, R.; Zhang, J.; Letsou, T.; Strangi, G.; Hinczewski, M.; Rawat, R. S.; Guo, C.; Singh, R. Generalized Brewster Angle Effect in Thin-Film Optical Absorbers and Its Application for Graphene Hydrogen Sensing. *ACS Photonics* **2019**, *6* (7), 1610−1617.
(41) Lee, S.; Seo, D.; Park, S. H.; Izquierdo, N.; Lee, E. H.; Younas, R.; Zhou, G.; Palei, M.; Hoffman, A. J.; Jang, M. S.; Hinkle, C. L.; Koester, S. J.; Low, T. Achieving Near-Perfect Light Absorption in Atomically Thin Transition Metal Dichalcogenides through Band Nesting. *Nature Communications 2023 14:1* **2023**, *14* (1), 1−9.
(42) Zhao, J.; Zhao, J.; Zhao, J.; Zhao, J.; Wang, Y.; Wang, Y.; Wang, Y.; Wang, Y.; Zhu, Y.; Zhang, W.; Zhang, W.; Yu, Y.; Yu, Y.; Yu, Y.; Yu, Y. Lithography-Free Flexible Perfect Broadband Absorber in Visible Light Based on an All-Dielectric Multilayer Structure. *Optics Letters* **2020**, *45* (19), 5464−5467.
(43) Justin Kunene, T.; Kwanda Tartibu, L.; Ukoba, K.; Jen, T. C. Review of Atomic Layer Deposition Process, Application and Modeling Tools. *Mater. Today Proc.* **2022**, *62*, S95−S109.
(44) Politano, G. G.; Versace, C. Spectroscopic Ellipsometry: Advancements, Applications and Future Prospects in Optical Characterization. *Spectroscopy Journal* **2023**, *1* (3), 163−181.
(45) Yoo, S. J.; Park, Q. H. Spectroscopic Ellipsometry for Low-Dimensional Materials and Heterostructures. *Nanophotonics* **2022**, *11* (12), 2811−2825.
(46) Amanollahi, M.; Moncada-Villa, E.; Zamani, M. Scattering Matrix Approach for Propagation of Electromagnetic Waves through Gyrotropic Superlens. *Physica B Condens Matter* **2021**, *615*, 413067.
(47) López-Medina, J.; Carvalho, W. O. F.; Vazquez-Arce, J.; Moncada-Villa, E.; Oliveira, O. N.; Farías, M. H.; Tiznado, H.; Mejía-Salazar, J. R. Refractive Index of ZnO Ultrathin Films Alternated with Al2O3 in Multilayer Heterostructures. *Nanotechnology* **2020**, *31* (50), 505715.
(48) Biesinger, M. C.; Payne, B. P.; Grosvenor, A. P.; Lau, L. W. M.; Gerson, A. R.; Smart, R. S. C. Resolving Surface Chemical States in XPS Analysis of First Row Transition Metals, Oxides and Hydroxides: Cr, Mn, Fe, Co and Ni. *Appl. Surf. Sci.* **2011**, *257* (7), 2717−2730.
(49) Nesbitt, H. W.; Banerjee, D. Interpretation of XPS Mn(2p) Spectra of Mn Oxyhydroxides and Constraints on the Mechanism of MnO2 Precipitation. *Am. Mineral.* **1998**, *83* (3−4), 305−315.
(50) Biesinger, M. C.; Lau, L. W. M.; Gerson, A. R.; Smart, R. S. C. Resolving Surface Chemical States in XPS Analysis of First Row Transition Metals, Oxides and Hydroxides: Sc, Ti, V, Cu and Zn. *Appl. Surf. Sci.* **2010**, *257* (3), 887−898.
(51) Barreca, D.; Battiston, G. A.; Berto, D.; Gerbasi, R.; Tondello, E. Y2O3 Thin Films Characterized by XPS. *Surface Science Spectra* **2021**, *8* (3), 234.
(52) Pirug, G.; Ritke, C.; Bonzel, H. P. Adsorption of H2O on Ru(001): II. Effect of Coadsorbed Alkali Metals (Na, K, Cs). *Surf. Sci.* **1991**, *257* (1−3), 50−62.
(53) Ringleb, F.; Fujimori, Y.; Wang, H. F.; Ariga, H.; Carrasco, E.; Sterrer, M.; Freund, H. J.; Giordano, L.; Pacchioni, G.; Goniakowski, J. Interaction of Water with FeO(111)/Pt(111): Environmental Effects and Influence of Oxygen. *J. Phys. Chem. C* **2011**, *115* (39), 19328−19335.
(54) Newberg, J. T.; Starr, D. E.; Yamamoto, S.; Kaya, S.; Kendelewicz, T.; Mysak, E. R.; Porsgaard, S.; Salmeron, M. B.; Brown, G. E.; Nilsson, A.; Bluhm, H. Formation of Hydroxyl and Water Layers on MgO Films Studied with Ambient Pressure XPS. *Surf. Sci.* **2011**, *605* (1−2), 89−94.
(55) Chiba, K.; Ohmori, R.; Tanigawa, H.; Yoneoka, T.; Tanaka, S. H2O Trapping on Various Materials Studied by AFM and XPS. *Fusion Eng. Des.* **2000**, *49−50*, 791−797.
(56) Payne, B. P.; Biesinger, M. C.; McIntyre, N. S. X-Ray Photoelectron Spectroscopy Studies of Reactions on Chromium Metal and Chromium Oxide Surfaces. *J. Electron Spectrosc. Relat. Phenom.* **2011**, *184* (1−2), 29−37.
(57) Dietl, T.; Ohno, H.; Matsukura, F.; Cibert, J.; Ferrand, D. Zener Model Description of Ferromagnetism in Zinc-Blende Magnetic Semiconductors. *Science (1979)* **2000**, *287* (5455), 1019−1022.
(58) Ciechan, A.; Bogusławski, P. Theory of the Sp-d Coupling of Transition Metal Impurities with Free Carriers in ZnO. *Scientific Reports 2021 11:1* **2021**, *11* (1), 1−11.
(59) Coey, J. M. D.; Venkatesan, M.; Fitzgerald, C. B.; Dorneles, L. S.; Stamenov, P.; Lunney, J. G. Anisotropy of the Magnetization of a Dilute Magnetic Oxide. *J. Magn Magn Mater.* **2005**, *290−291*, 1405−1407.
(60) Wei, X.; Skomski, R.; Balamurugan, B.; Sun, Z. G.; Ducharme, S.; Sellmyer, D. J. Magnetism of TiO and TiO_2 Nanoclusters. *J. Appl. Phys.* **2009**, *105* (7), 07C517 DOI: 10.1063/1.3074509.
(61) Kanwal, S.; Tahir Khan, M.; Tirth, V.; Algahtani, A.; Al-Mughanam, T.; Zaman, A. Room-Temperature Ferromagnetism in Mn-Doped ZnO Nanoparticles Synthesized by the Sol-Gel Method. *ACS Omega* **2023**, *8* (31), 28749−28757.
(62) Coey, J. M. D.; Venkatesan, M.; Fitzgerald, C. B. Donor Impurity Band Exchange in Dilute Ferromagnetic Oxides. *Nature Materials 2005 4:2* **2005**, *4* (2), 173−179.
(63) Meng, H. J.; Hou, D. L.; Jia, L. Y.; Ye, X. J.; Zhou, H. J.; Li, X. L. Role of Oxygen Vacancies on Ferromagnetism in Fe-Doped TiO_2 Thin Films. *J. Appl. Phys.* **2007**, *102* (7), 073905 DOI: 10.1063/1.2786115.
(64) Zhang, J.; Skomski, R.; Lu, Y. F.; Sellmyer, D. J. Temperature-Dependent Orbital-Moment Anisotropy in Dilute Magnetic Oxides. *Phys. Rev. B Condens Matter Mater. Phys.* **2007**, *75* (21), 214417.

(65) Luo, X.; Lee, W. T.; Xing, G.; Bao, N.; Yonis, A.; Chu, D.; Lee, J.; Ding, J.; Li, S.; Yi, J. Ferromagnetic Ordering in Mn-Doped ZnO Nanoparticles. *Nanoscale Res. Lett.* **2014**, *9* (1), 625.
(66) Panda, J.; Sasmal, I.; Nath, T. K. Magnetic and Optical Properties of Mn-Doped ZnO Vertically Aligned Nanorods Synthesized by Hydrothermal Technique. *AIP Adv.* **2016**, *6* (3), 35118.

https://doi.org/10.1021/acsanm.4c06418
ACS Appl. Nano Mater. 2025, 8, 4441−4452